

## Customized Three-dimensional Computational Fluid Dynamics Simulation of the Upper Airway of Obstructive Sleep Apnea

Sang-Jin Sung<sup>a</sup>; Soo-Jin Jeong<sup>b</sup>; Yong-Seok Yu<sup>c</sup>; Chung-Ju Hwang<sup>d</sup>; Eung-Kwon Pae<sup>e</sup>

### ABSTRACT

**Objective:** To use computer simulations to describe the role of fluid dynamics in the human upper airway.

**Materials and Methods:** The model was constructed using raw data from three-dimensional (3-D) computed tomogram (CT) images of an obstructive sleep apnea (OSA) patient. Using Bionix<sup>®</sup> software (CantiBio Inc., Suwon, Korea), the CT data in DICOM format was transformed into an anatomically correct 3-D Computational fluid dynamic (CFD) model of the human upper airway. Once constructed, the model was meshed into 725,671 tetra-elements. The solution for testing was performed by the STAR-CD software (CD adapco group, New York, NY). Airflow was assumed to be turbulent at an inspiration rate of 170, 200, and 230 ml/s per nostril. The velocity magnitude, relative pressure, and flow distribution was obtained.

**Results:** High airflow velocity predominated in medial and ventral nasal airway regions. Maximum air velocity (15.41 m/s) and lowest pressure (negative 110.8 Pa) were observed at the narrowest portions of the velopharynx. Considering differences in model geometry, flow rate, and reference sections, when airflow patterns in nasal cavity were compared, our results were in agreement with previous data.

**Conclusions:** CFD analyses on airway CT data enhanced our understanding of pharyngeal aerodynamics in the pathophysiology of OSA and could predict the outcome of surgeries for airway modification in OSA patients.

**KEY WORDS:** Upper airway; 3-dimensional customized models; Computational fluid dynamics

### INTRODUCTION

Soft tissue compliance and reduced intraluminal pressure in the airway during inspiratory effort may

play a crucial role in airway occlusion in the pathogenesis of obstructive sleep apnea (OSA).<sup>1-3</sup> A lengthened pharyngeal airway<sup>4-6</sup> and a reduced velopharynx to hypopharynx cross-sectional area ratio<sup>6-8</sup> contribute to the pathogenesis of OSA. Nasal obstruction may aggravate the symptoms of OSA as well.<sup>9,10</sup>

Because maximum airflow velocity and pressure gradients are found at the minimal cross-sectional area of a conduit, compensatory effort to overcome a narrow airway and to maintain tidal volume becomes critical in OSA patients.<sup>11</sup> When a given air volume must traverse a smaller cross-sectional area more rapidly, pressure may be further reduced.<sup>4</sup> Pressure becomes an important factor in mediating airway obstruction because reduced pressure in the presence of rapid airflow leads to adduction of the surrounding tissue.

Flow patterns in nasal airway have been studied using a plexiglas model with dye injection at steady flow or by Computational Fluid Dynamics (CFD). Hahn et

<sup>a</sup> Assistant Professor, Department of Orthodontics, University of Ulsan College of Medicine, Asan Medical Center, Seoul, South Korea.

<sup>b</sup> Assistant Professor, Department of Automotive Engineering, Donghae University, Gangwon, South Korea.

<sup>c</sup> Research Director, CANTIBio INC. BME, Suwon, South Korea.

<sup>d</sup> Professor and Department Chair, Department of Orthodontics, College of Dentistry, Yonsei University, Seoul, South Korea.

<sup>e</sup> Assistant Professor, Section of Orthodontics, UCLA School of Dentistry, Los Angeles, Calif.

Corresponding author: Dr. Eung-Kwon Pae, Section of Orthodontics, UCLA School of Dentistry 43-091 CHS 10833, Le Conte Ave, Los Angeles, CA 90095-1668 (e-mail: epae@dent.ucla.edu)

Accepted: September 2005. Submitted: July 2005.

© 2006 by The EH Angle Education and Research Foundation, Inc.

**Table 1.** Physical and Sleep Characteristics of the Subject<sup>a</sup>

Physical Data	Sleep Data
Height, 169.3 cm	RDI (counts/h), 9.4
Weight, 66 kg	AI (counts/h), 9.47
BMI, 23.8	Desaturation index (desat/h), 3.2
	Number of desaturations, 22
	Desaturation minimum (%), 82.9
	Desaturation maximum (%), 86.7

<sup>a</sup> RDI indicates respiratory disturbance index; BMI, body mass index; weight, kg/height<sup>2</sup> in m<sup>2</sup>; AI, Apnea index.

al<sup>12</sup> used a 20-fold enlarged model to measure the airflow pattern. Keyhani et al<sup>13</sup> constructed a CFD model of the same geometry and compared the experimental and calculated outcomes. The CFD model by Subramaniam et al<sup>14</sup> studied another clinically relevant aspect, a human nasopharynx with a significant bend. To our knowledge, despite all previous efforts, no computational study exists which analyzes a three-dimensional (3-D) upper airway model including the nasal cavity and pharynx.

Fluid dynamics examines parameters such as velocity and flow path.<sup>12–16</sup> In humans, turbulent flow is generated in the airflow path from the nostrils to the hypopharynx by several anatomical structures, including the two nasal valves, three turbinates, and the epiglottis.<sup>12,17</sup> The turbulent flow exhibits a flow regime characterized by pressure and velocity variations with time (ie, nonpredictable swirl).

The pathophysiology of OSA is not yet fully understood. Previous modeling was limited to unilateral nasal cavity or part of the upper airway.<sup>13,18,19</sup> 3-D CFD models, including the nasal cavity and pharynx, were previously constructed, yet without computational simulation.<sup>20</sup> One of the constructed models was analyzed as a function of flow rates.<sup>13,14,18</sup> This study uses 3-D human pharyngeal airway CFD models automatically generated using commercial software and a finite volume method based on the CT of an OSA patient. The airflow velocity, particle streak line, and negative pressure in the upper airway were calculated and compared with previous studies to validate our CFD analyses.

## MATERIALS AND METHODS

Computed tomogram (CT) data obtained from a 37-year-old male patient with mild OSA symptoms were examined by computer modeling for this study (Table 1). Protocols for the study were approved by the local hospital committee on clinical investigation, and informed consent was obtained from the patient.

3-D CT scanning was performed on a General Electric Light Speed QX/i (Wis) scanning station with the following parameters: 120 kVp, 360 mA, rotation time

of 0.5 seconds, pitch 3, thickness 1.25 mm, HQ mode. Scanning was conducted (the patient was awake and reclining) at the end point of the expiration from the supraorbital margin through the two cm inferior to the hyoid bone, as described previously.<sup>21</sup>

## Computer Modeling and 3-D Mesh Generation

The scanned images were transferred to Bionix Body builder software (version 3.0, CANTIBio Inc, Suwon, Korea). The segments of interest were reconstructed into 3-D images. The airway region was isolated from other structures by the built-in threshold and segmentation function. The range of 0 to 800 threshold level was applied to the area consisting of air. The frontal, ethmoidal, and paranasal sinuses and oral cavity were erased by manual editing.<sup>22</sup>

HyperMesh software (version 5.0, Altair Engineering, Troy, Minn) was used to mesh the inside of the 3-D surface with the tetrahedron element with the options of standard growth and normal mesh generation. The finished original upper airway model was composed of 725,671 elements with 167,089 nodal points.

## Representative Sections and Anatomy of Nasal Airway

The magnitude of airflow velocity in the nasal cavity was calculated at the five different cross-sections shown in Figure 1, panel A. The regions of the nasal airway were designated using nomenclature proposed by Proctor.<sup>17</sup> Section 1 is located between the end of the nasal vestibule and the beginning of the main nasal passage. The middle and inferior turbinate begin at section 2, whereas section 3 is located in the middle of the nasal passage showing the most convoluted cross-section. The two nasal cavities merge posterior to section 4, and section 5 constitutes the end of the nasal passage and the beginning of the nasopharynx. Directional airflow changes from horizontal to vertical toward the oropharynx. Additional cross-sections were selected to inspect the obstruction area of the pharynx. The narrowest portion of the velopharynx was observed in lateral view, and section 6 was constructed perpendicular to the longitudinal axis of the airway (Figure 1, panel A). Section 7 shows the midsagittal plane of the upper airway as it extends from the nasopharynx to the hypopharynx.

Each element on the entrance of each nostril was considered a flow inlet and the elements on the exit plane of the hypopharynx were defined as flow outlets (Figure 1, panels B and C). The medial airways (close to the nasal septum) were subdivided into middle medial airway (mma) and inferior medial airway (ima) (Figure 1, panel D). The orientation of the CFD model is also depicted in Figure 1, panels A and B.

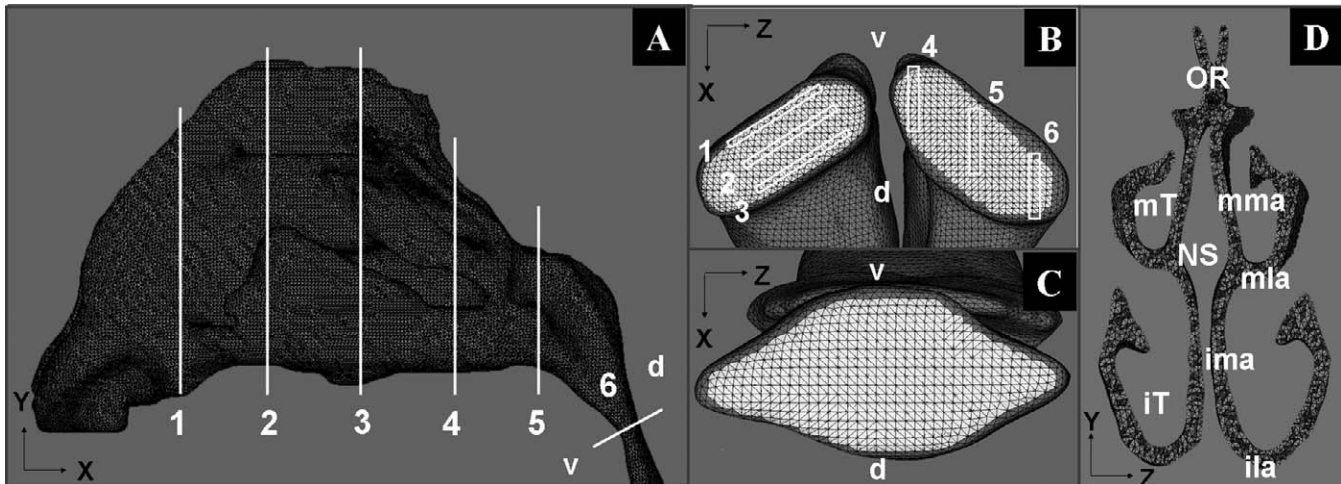


**Figure 1.** Anatomy of the nasal airway for the CFD model. (A) Lateral view of the nasal cavity and the pharynx with six representative sections. (B) Inferior view of the nostrils, ie, flow-inlet areas divided by six particle-releasing compartments. (C) Flow-outlet area of the hypopharynx. (D) The nasal airway was subdivided into mma, middle medial airway; ima, inferior medial airway; mla, middle lateral airway; ila, inferior lateral airway. OR, Olfactory region; mT, middle turbinate region; iT, inferior turbinate region; NS, nasal septum; v, ventral; and d, dorsal sides are shown.

### Computational Approach

The Governing equations and Boundary conditions are detailed in the Appendix 1. Our study simulates turbulent flow to estimate virtual airflow patterns in the pharyngeal airway. The simulations were performed by the STAR-CD software (CD Adapco group, New York, NY) and run on a PC, Pentium 4 CPU (2.66 GHz) with 1 G byte RAM and calculated at a flow rate of 170, 200, and 230 ml/s.

### Validation of the Airflow Patterns in the Nasal Cavity

To examine the validity of our CFD results, the airflow patterns in the nasal cavity were compared with the previously published data at a flow rate of 200 ml/s. The axial airflow velocity ( $V_x$ ) in the nasal cavity represents the velocity component for the ventrodorsal direction. The velocity magnitude was calculated by integrating the velocity for the  $x$ ,  $y$ ,  $z$  directions ( $=\sqrt{V_x^2 + V_y^2 + V_z^2}$ ). Particle streak lines visualizing the airflow path were computed as visualized patterns formed by dye or buoyant particles released into the nostril of the model at steady flow. Six compartments were used in our nasal cavity model (Figure 1, panel B). An isovelocity surface contour was used to demonstrate distribution patterns of airflow velocity on the surface of CFD models calculated by interpolation of the velocity on the airway wall and on the inside of the airway.

### RESULTS

#### Airflow Pattern in the Nasal Cavity at a Flow Rate of 200 mL/s

The maximum velocity magnitude that is integrated velocity in section 1 was 3.267 m/s in the left nasal cavity at 8 mm above the nasal floor and 1.867 m/s in the right nasal cavity at 11.3 mm above the nasal floor as shown in Figure 2. The maximum axial velocity ( $V_x$ ), however, was 2.695 m/s in the left nasal cavity and 1.403 m/s in the right. As a consequence of the secondary flow ( $V_y$ ,  $V_z$ ) developed because of airway geometry, the maximum axial velocity was lower than the maximum velocity magnitude. The secondary flows provide an indication of swirling airflows in the nasal cavity. In section 2, the maximum velocity was reduced to 2.691 m/s. High velocity magnitude was observed in the inferior medial airway and inferior lateral airway.

Although the cross-section of the nasal cavity in section 3 was more complex, the maximum velocity magnitude calculated at the junction of the middle medial and middle lateral airway and inferior medial airway was reduced to 1.922 m/s. The maximum axial velocity was 1.904 m/s and the amount of secondary flow was also reduced. This airflow pattern occurred similarly in section 4. The maximum velocity magnitude (2.735 m/s) of section 5 was observed at the nasal floor, but the velocity magnitude (0.195 m/s) was significantly reduced near the roof of the airway. As the secondary flows increased, the difference between the maximum velocity magnitude and the maximum axial velocity was increased to 0.48 m/s as well.

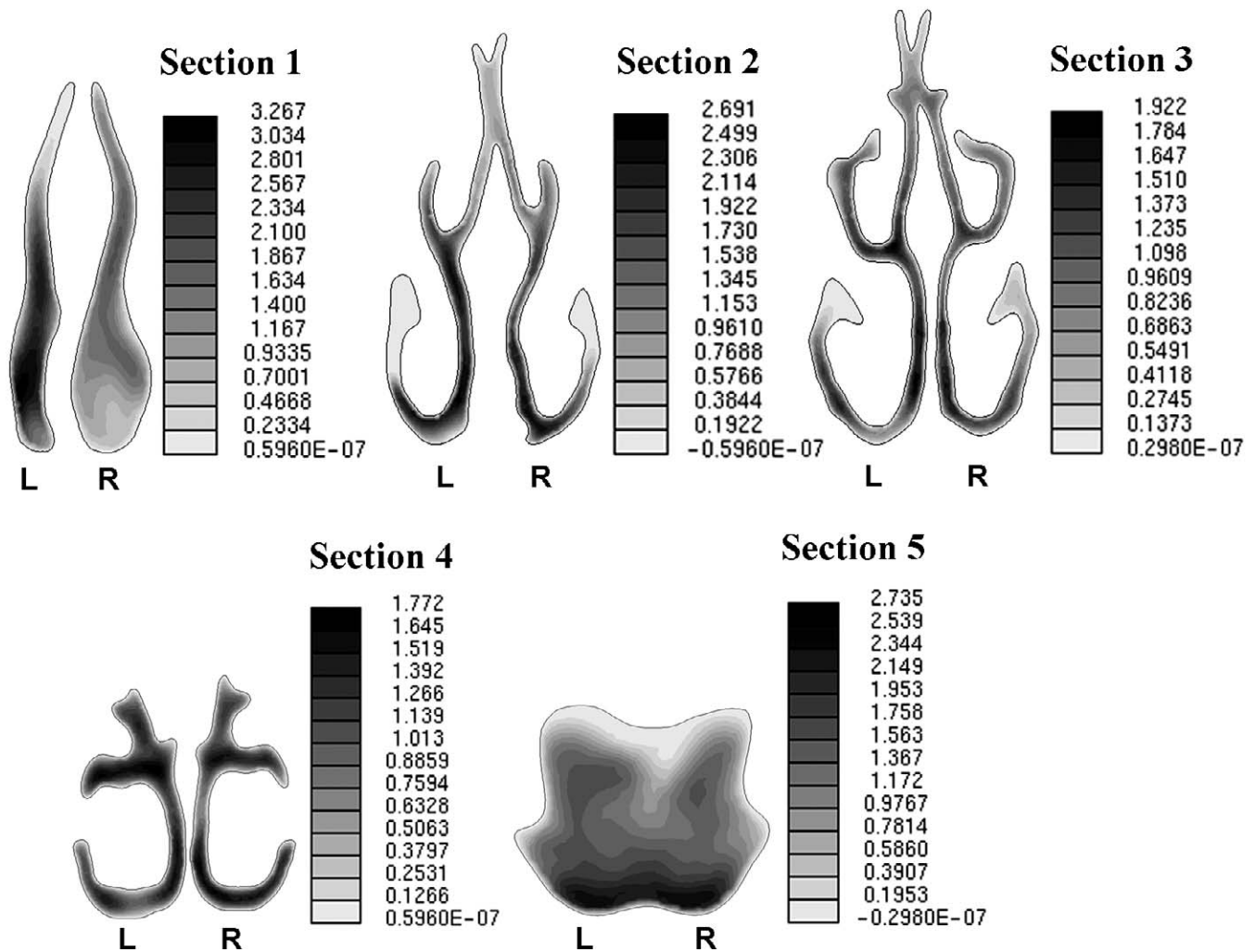


**Figure 2.** Isovelocity contours for velocity magnitudes in the nasal cavity (expressed in m/s) for the five sections. L and R indicate left and right sides.

Figure 3 exhibits simulated particle streak lines generated by the particles released from compartment 1–6 (See Figure 1, panel B). The particles from compartment 1 in Figure 1B were initially directed upward toward the olfactory region and deflected toward the nasopharynx. The particle streak lines generated by the particles from compartment 2 demonstrated evenly distributed flows toward the nasal roof and over the nasal floor. All particle streak lines for compartment 3 float immediately above the nasal floor. Airflow paths for compartment 4 were distributed in the nasal roof, yet the particle streak lines show the air stream from compartment 6 passes mainly over the nasal floor.

The particle streak lines on the ventral side of the pharynx originated from compartments 1 and 3 and mainly from compartments 4 and 5 on the dorsal side, as shown in Figure 3. The shortest flow path from the nostril to the hypopharynx originated from compartment 3 and the longest path from compartment 4.

#### Airflow Pattern in the Pharynx at a Flow Rate of 200 mL/s

The maximum velocity magnitude (15.41 m/s) in the pharyngeal airway was observed at the level of section 6 (Figure 1, panel A) and was located in the right side of the ventral surface of the model (Figure 4, panels A and C). Relatively high velocities were observed in the uvula region as Figure 4, panel A indicates. The isovelocity contour of section 6 was circular, and the fluid velocity approaches zero close to the wall (Figure 4, panel C), presumably because of the air viscosity to the pharyngeal wall. The maximum negative pressure (–110.8 Pa) also occurs on section 6. The isopressure contour, as well as the isovelocity magnitude contour, was eccentrically layered as shown in Figure 4, panel D.

As shown in Figure 5, as the airflow rate increased from 170 to 230 ml/s, the maximum velocity magnitude

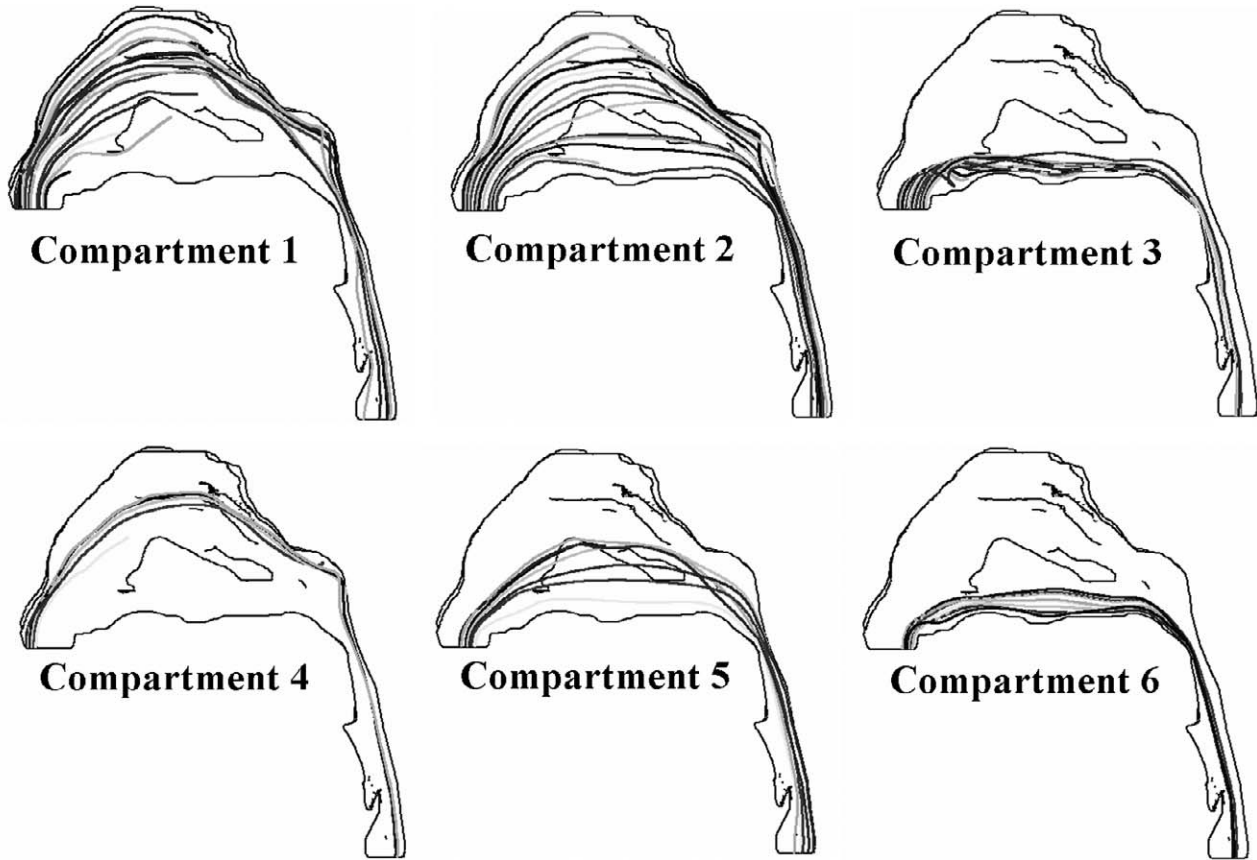


Figure 3. Particle streak lines from six particle-releasing compartments.

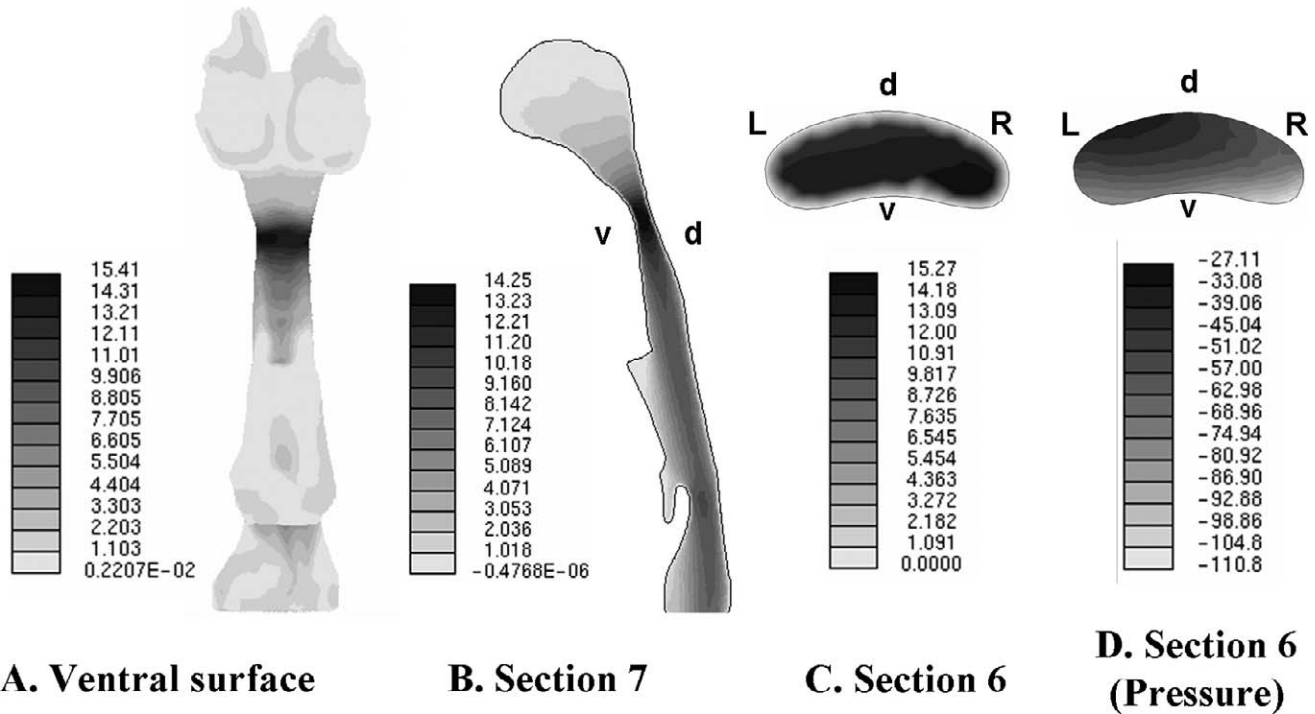
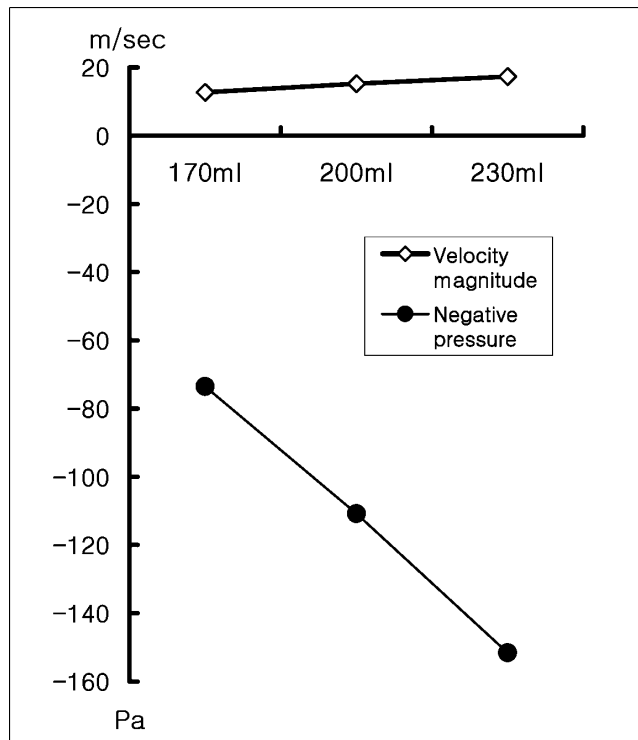


Figure 4. Airflow patterns of the pharynx at a flow rate of 200 ml/s. Velocity magnitudes (unit: m/s) of the ventral surface (A), of section 7 (B), and of section 6 (C). Pressure distribution, section 6 (D). L, R, d, and v represent left, right, dorsal, and ventral sides.



**Figure 5.** Comparisons of the maximum velocity magnitude and negative pressures on section 6 at a flow rate of 170, 200, and 230 mL/s.

increased from 12.73 to 17.31 m/s and the negative pressure decreased from  $-73.57$  to  $-151.6$  Pa. The change of the velocity magnitude and negative pressure were not in proportion to the increase of flow rate.

## DISCUSSION

Analysis of the anatomically correct CFD computer models of the human upper airway based on CT images may provide a unique opportunity to study airway aerodynamics in OSA patients. Customized CFD modeling is less invasive because studying in vitro models, after once constructed, no longer involves human subjects and is versatile because it allows studying inter-individual variations. Despite differences in model ge-

ometry, flow rate, and reference sections, our results on airflow patterns in nasal cavity are in agreement with previous data (Table 2).

Air flow in the region below the inferior turbinate appeared to originate from the posterior part of the nostril. Air streams close to the nasal septum around the anterior portion of the nostril tend to rise vertically, then deflect toward the floor. Most dorsal streams appear to originate from the anterior portion of nostril. Our study confirms previous findings that airflow in the nasal floor originates from the dorsal half of the nostril and the flow in the nasal roof area, including dorsal olfactory region, from the ventral half.<sup>13,14,23</sup>

The nasal valve area is considered the narrowest and most collapsible region in the nasal cavity. The nasal valve cross-sectional area that is 55–100 mm<sup>2</sup> per side acts as a flow-limiting structure when inspiratory rates exceed 500 ml/s.<sup>24,25</sup> In contrast, the velopharynx in OSA patients is regarded as the most collapsible region of the upper airway and the flow-limiting structure during sleep. Schwab et al<sup>21</sup> reported CT data showing that the retropalatal area was approximately 90 mm<sup>2</sup> for a snorer/mild apneic subject and 50 mm<sup>2</sup> for an apneic subject, whereas the cross-sectional areas for the velopharynx in our model was approximately 52 mm<sup>2</sup>. As Poiseuille's law states, airflow through a conduit is inversely proportional to the fourth power of the radius.<sup>26</sup> The reduced cross-sectional area at the velopharyngeal area in OSA patients is expected to have an exponential effect on airflow and airway resistance.<sup>11</sup> Thus, inspiratory effort to maintain tidal volume against increased airway obstruction would further decrease intrathoracic pressure.<sup>10,27</sup> Our results suggest that reduced cross-sectional area at the velopharyngeal area appears to be a major contributor in the pathophysiology of OSA.

Our results show that the maximum velocity magnitude in the nostril (3.4 m/s from surface velocity contour) increased markedly at the minimum cross-sectional area at the velopharyngeal area (15.27 m/s, section 6), as expected; the maximum negative pressure was  $-110.8$  Pa (Figure 4, panels C and D). The se-

**Table 2.** Comparison of the Airflow Velocities in the Nasal Cavity with the Previous Studies<sup>a</sup>

	Geometry	Method	Flow rate (ml/s)	Maximum Flow Velocity at Cross-section (m/s)			
				A	B	C	D
Hahn et al (12)	Rt	Experiment	180	2.6	1.8	1.47	1.25
Keyhani et al (13)	Rt	CFD	180	2.5	1.9	1.54	1.38
Subramaniam et al (14)	Rt and Lt	CFD	250	3.89	3.34	2.73	2.59
This study	Rt and Lt	CFD	200	2.8–3.2	1.9–2.1	1.51–1.65	1.2–1.3

<sup>a</sup> Flow rate: ml/s per nostril. Cross-section: A, B, C, and D represent Sections 1 to 4 in this study. Rt: Right nasal cavity, Lt: Left nasal cavity. This study: velocity of this study was cited from contour plot in Figure 3 and described as range. All velocity values of the other studies observed near our cross-sections were chosen.

verely decreased upper airway pressure may result in a collapse of the velopharynx in OSA patients.

The eccentrically distributed velocity and pressure observed in section 6 (Figure 4, panels C and D) could be caused by the airflow passing through different geometries of the right and left nasal cavity, swirling of right and left nasal airflows joining into the nasopharynx, and the flow change at the transition of the nasopharyngeal area into the oropharynx at an angle of approximately 90°.

Our study reports the dynamic changes of airflow pattern during inspiratory phase in a given static geometry, not in dynamic changes of the geometry during inspiration and expiration. Although CFD meshing with a hexahedron element may be a current trend, our meshing technique using tetrahedron elements shows an advantage of anatomically correct, automatic and rapid meshing. Nevertheless, our results suggest that customized CFD simulation models for the upper airway may be a useful tool to study OSA and predict the treatment outcome of multilevel airway modifications in OSA patients.

## CONCLUSIONS

CFD analyses on airway CT data enhance our understanding of pharyngeal aerodynamics in the pathophysiology of OSA and could predict the outcome of surgeries for airway modification in OSA patients.

## ACKNOWLEDGMENTS

This study was supported by grants from Asan Institute for Life Science (Grant #2005-292) and the Dean's Seed Grant Program of the UCLA School of Dentistry (E.P.).

## REFERENCES

1. Remmers JE, deGroot WJ, Sauerland EK, Anch AM. Pathogenesis of upper airway occlusion during sleep. *J Appl Physiol.* 1978;44:931–938.
2. Leiter JC. Upper airway shape: is it important in the pathogenesis of obstructive sleep apnea? *Am J Respir Crit Care Med.* 1996;153:894–898.
3. Fogel RB, Malhotra A, White DP. Sleep 2: pathophysiology of obstructive sleep apnoea/hypopnoea syndrome. *Thorax.* 2003;59:159–163.
4. Pae EK, Lowe AA, Fleetham JA. A role of pharyngeal length in obstructive sleep apnea patients. *Am J Orthod Dentofacial Orthop.* 1997;111:12–17.
5. Malhotra A, Huang Y, Fogel RB, Pillar G, Edwards JK, Kikinis R, Loring SH, White DP. The male predisposition to pharyngeal collapse: importance of airway length. *Am J Respir Crit Care Med.* 2002;166:1388–1395.
6. Liao YF, Huang CS, Chuang ML. The utility of cephalometry with the Muller maneuver in evaluating the upper airway and its surrounding structures in Chinese patients with sleep disordered breathing. *Laryngoscope.* 2003;113:614–619.
7. Polo OJ, Tafti M, Fraga J, Porkka KV, Dejean Y, Billiard M. Why don't all heavy snorers have obstructive sleep apnea? *Am Rev Respir Dis.* 1991;143:1288–1293.
8. Lam B, Ooi CG, Peh WC, Lauder I, Tsang KW, Lam WK, Ip MS. Computed tomographic evaluation of the role of craniofacial and upper airway morphology in obstructive sleep apnea in Chinese. *Respir Med.* 2004;98:301–307.
9. Corey JP, House RSM, Ng BA. Nasal congestion: a review of its etiology, evaluation, and treatment. *Ear Nose Throat J.* 2000;79:690–693.
10. Rappai M, Collop N, Kemp S, deShazo R. The nose and sleep-disordered breathing: what we know and what we do not know. *Chest.* 2003;124:2309–2323.
11. Isono S, Feroah TR, Hajduk EA, Brant R, Whitelaw WA, Remmers JE. Interaction of cross-sectional area, driving pressure, and airflow of passive velopharynx. *J Appl Physiol.* 1997;83:851–859.
12. Hahn I, Scherer PW, Mozell MM. Velocity profiles measured for airflow through a large-scale model of the human nasal cavity. *J Appl Physiol.* 1993;75:2273–2287.
13. Keyhani K, Scherer PW, Mozell MM. Numerical simulation of airflow in the human nasal cavity. *J Biomech Eng.* 1995;117:429–441.
14. Subramaniam RP, Richardson RB, Morgan KT, Kimbell JS. Computational fluid dynamics simulations of inspiratory airflow in the human nose and nasopharynx. *Inhalation Toxicology.* 1998;10:473–502.
15. Schreck S, Sullivan KJ, Ho CM, Chang HK. Correlations between flow resistance and geometry in a model of the human nose. *J Appl Physiol.* 1993;75:1767–1775.
16. Kelly JT, Prasad AK, Wexler AS. Detailed flow patterns in the nasal cavity. *J Appl Physiol.* 2000;89:323–337.
17. Proctor DF. The upper airways. I. Nasal physiology and defense of the lungs. *Am Rev Respir Dis.* 1997;115:97–129.
18. Li WI, Perzl M, Heyder J, Langer R, Brain JD, Englmeier KH, Niven RW, Edwards D. Aerodynamics and aerosol particle deaggregation phenomena in model oral-pharyngeal cavities. *J Aerosol Sci.* 1996;27:1269–1286.
19. Katz IM, Davis BM, Martonen TB. A numerical study of particle motion within the human larynx and trachea. *J Aerosol Sci.* 1999;30:173–183.
20. Martonen TB, Zhang Z, Yu G, Musante CJ. Three-dimensional computer modeling of the human upper respiratory tract. *Cell Biochem Biophys.* 2001;35:255–261.
21. Schwab RJ, Gefte WB, Hoffman EA, Gupta KB, Pack AI. Dynamic upper airway imaging during awake respiration in normal subjects and patients with sleep disordered breathing. *Am Rev Respir Dis.* 1993;148:1385–1400.
22. Aykac D, Hoffman EA, McLennan G, Reinhardt JM. Segmentation and analysis of the human airway tree from three-dimensional X-ray CT images. *IEEE Trans Med Imaging.* 2003;22:940–950.
23. Masing H. Experimental studies on the flow in a nose model. *Arch Klin Exp Ohren Nasen Kehlkopfheilkd.* 1967;189:371–381.
24. Hilberg O, Jackson AC, Swift DL, Pedersen OF. Acoustic rhinometry: evaluation of nasal cavity geometry by acoustic reflection. *J Appl Physiol.* 1989;66:295–303.
25. Schlosser RJ, Park SS. Functional nasal surgery. *Otolaryngol Clin North Am.* 1999;32:37–51.
26. Yang C, Woodson BT. Upper airway physiology and obstructive sleep-disordered breathing. *Otolaryngol Clin North Am.* 2003;36:409–421.
27. Gleeson K, Zwillich CW, White DP. The influence of increasing ventilatory effort on arousal from sleep. *Am Rev Respir Dis.* 1990;142:295–300.
28. Chang HK. Flow dynamics in the respiratory tract. In: Chang HK, Paiva M, eds. *Respiratory Physiology, An Analytical Approach.* New York, NY: Dekker; 1989:57–138.

29. Yakhot V, Orszag SA. Renormalization group analysis of turbulence, I. Basic theory. *J Sci Comput.* 1986;1:1–16.
30. STAR-CD Ver. 3.15 Manual, 2000, Computational Fluid Dynamics Ltd.
31. Rhie RM, Chow WL. Numerical study of the turbulent flow past an airfoil with trailing edge separation. *Inst Aeronaut Astronaut J.* 1983;21:1525–1537.
32. Patankar SV, Spaldin DB. A calculation procedure for heat, mass and momentum transfer in three-dimensional parabolic flows. *Int J Heat Mass Transfer.* 1972;15:1778–1806.
33. Launder BE, Spalding DB. The numerical computation of turbulent flows. *Comput Methods Appl Mech Eng.* 1974;3: 269–289.

## APPENDIX 1

### Nomenclature

$\omega$ :	Angular breathing frequency
$L$ :	Axial length of the model
$U_{in}$ :	Average velocity at the inlet
$\rho$ :	Air mass density
$\mu_o$ :	Intrinsic air viscosity
$v$ :	Air velocity vector
$k$ :	Turbulent kinetic energy
$\varepsilon$ :	Dissipation rate of turbulent kinetic energy
$\nu_{mol}$ :	Molecular dynamic viscosity
$C_{\mu}, C_{\varepsilon 1}, C_{\varepsilon 2}$ :	0.085, 1.42, and 1.68, respectively
$k_{in}$ :	Turbulence energy at inlet
$I$ :	Intensity of turbulence (=0.12)
$\varepsilon_{in}$ :	Turbulence energy dissipation at inlet
$C_{\mu}$ :	Experimental constant (=0.09)
$R$ :	Characteristic length ( $=\sqrt{A_{in}/\pi}$ )
$A_{in}$ :	Area at inlet section
$P$ :	Pressure (Pa in atmosphere)
$u_i$ :	Mean velocity components in Cartesian coordinates
$x, y, z$ :	Coordinate axes
$x_i$ :	Coordinate direction

### Governing Equations

Airflow inside a human nasal cavity is in a dynamic state; ie, it decelerates and accelerates from a resting state during normal breathing.<sup>12</sup> For a quiet restful breathing frequency of 0.25 Hz and half-nasal flow rate of less than 200 mL/s, the Strouhal number ( $=\omega L/U_{in}$ ), from which the importance of unsteadiness for the developing flow in the finite length of the nasal cavity can be estimated, is less than 0.2, indicating that a quasi-steady approximation is reasonable.<sup>13</sup> Other previous study has also concluded that nasal airflow can be considered as steady or quasisteady in most conditions.<sup>28</sup> For an incompressible steady flow with constant viscosity, Reynolds-averaged governing equations for momentum can be written in the following form:

$$\rho \frac{\partial}{\partial x_j} (u_j u_i) = \frac{\partial}{\partial x_j} \left( \mu \frac{\partial u_i}{\partial x_j} \right) + S_{\phi} \quad (1)$$

where

$$S_{\phi} = -\frac{\partial p}{\partial x_i} + \frac{\partial}{\partial x_j} \left( \mu \frac{\partial u_j}{\partial x_i} \right)$$

The above equations, called Navier-Stokes equations, have been altered from their laminar counterparts by replacing the intrinsic shear viscosity  $\mu_o$  with the effective (time-averaged) viscosity

$$\mu = \mu_o + \mu_t$$

where

$$\mu_t = \rho C_{\mu} \frac{k^2}{\varepsilon}$$

is the turbulent viscosity. To compute variables  $k$  and  $\varepsilon$ , the RNG  $k - \varepsilon$  turbulent model<sup>29</sup> was used:

$$\rho \frac{\partial (u_j k)}{\partial x_j} = \frac{\partial}{\partial x_j} \left( \alpha_k \rho \mu \frac{\partial k}{\partial x_j} \right) + \rho \mu_t \left( \frac{\partial u_i}{\partial x_j} + \frac{\partial u_j}{\partial x_i} \right) \frac{\partial u_i}{\partial x_j} - \rho \varepsilon \quad (2)$$

$$\rho \frac{\partial (u_j \varepsilon)}{\partial x_j} = \frac{\partial}{\partial x_j} \left( \alpha_{\varepsilon} \rho \nu_{eff} \frac{\partial \varepsilon}{\partial x_j} \right) + C_{\varepsilon 1} \frac{\varepsilon}{k} \rho \mu_t \left( \frac{\partial u_i}{\partial x_j} + \frac{\partial u_j}{\partial x_i} \right) \frac{\partial u_i}{\partial x_j} - C_{\varepsilon 2} \rho \frac{\varepsilon^2}{k} - R \quad (3)$$

where

$$\nu_{eff} = \nu_{mol} \left( 1 + \frac{\sqrt{\nu_t}}{\nu_{mol}} \right)^2, \quad R = \frac{C_{\mu} \rho \eta^3 \left( 1 - \frac{\eta}{4.38} \right) \varepsilon^3}{1 + 0.012 \eta^3 \frac{\varepsilon^3}{k}},$$

$$\eta = \frac{1}{2} \left( \frac{\partial u_i}{\partial x_j} + \frac{\partial u_j}{\partial x_i} \right) \frac{k}{\varepsilon}$$

Turbulent airway flow governed by the above equations (1) to (3) was calculated by a CFD package, STAR-CD version 3.15 of Adapco, UK,<sup>30</sup> finite volume solver using body-fitted grids. The grids are nonstaggered and all variables are to be evaluated at the center of each cell. The Rhie and Chow algorithm<sup>31</sup> was used to calculate the velocity at the cell faces. A MARS (Monotone advection and reconstruction scheme), second-order accurate differencing scheme was used in the “discretization” of the governing equations 1–3.<sup>30</sup> Of all differencing schemes available in STAR-CD, MARS was chosen for its optimal sensitivity to the solution accuracy for the mesh structure and skew. The Semi-Implicit Method for Pressure-Linked Equations (SIMPLE) algorithm<sup>32</sup> was used to manage the pressure-velocity coupling. To stabilize the solution, underrelaxation factors were used for all the basic variables.

### Boundary Conditions

We assumed that the uniform velocity profile and the axial component of velocity were perpendicular to the flow inlet faces. At the inlets, the turbulence kinetic energy  $k$  and its dissipation rate  $\varepsilon$  were calculated as

$$k_{in} = \frac{3}{2}(I \cdot U_{in})^2, \quad \varepsilon_{in} = \frac{C_{\mu}^{0.75} \cdot k_{in}}{0.007R}$$

A No-slip condition was imposed on the walls, and the

standard wall function<sup>33</sup> was used with the RNG  $k - \varepsilon$  model. A constant atmospheric pressure condition was imposed at the outlet boundary. The velocities at outlet were linked to the local pressure gradients by special momentum equations whose coefficients were equated to those at the cell center. These equations, together with the continuity constraint, effectively allowed the magnitude and direction of the local flow (which may be inwards or outwards) to be calculated.<sup>30</sup>